



# Plasmon-mediated activation of persulfate for efficient photodegradation of ionic liquids over Ag@Pd core-shell nanocubes

Li Zhang, Weiwei Lu<sup>\*</sup>, Peng Xu, Hao Wang, Xuefeng Wei, Kaisheng Yao<sup>\*</sup>, Shuge Peng<sup>\*</sup>

School of Chemical Engineering and Pharmaceuticals, Henan University of Science and Technology, Luoyang, Henan 471003, PR China

## ARTICLE INFO

### Keywords:

Ionic liquids  
Plasmonic catalyst  
Sulfate radical  
EPR technique  
Advanced oxidation process

## ABSTRACT

In this study, we propose a novel photo-activation method to remove persistent organic pollutants through a  $\text{SO}_4^{\cdot-}$ -based advanced oxidation process. Core-shell Ag@Pd nanocubes were prepared by a facile seed-mediated method and, afterward, explored for photodegradation of a representative ionic liquid (IL), [C<sub>4</sub>mim]Br. Electron paramagnetic resonance measurements and radical scavenging experiments demonstrated that the species mainly responsible for degrading [C<sub>4</sub>mim]Br were the radicals of  $\text{SO}_4^{\cdot-}$ . The plasmon-mediated nature of the Ag@Pd catalysts was verified by their wavelength-dependent performance. Subsequent optical simulation indicated that, other than the plasmonic Ag core, the non-plasmonic Pd shell was the preferential site for dissipating the absorbed photons into energetic charge carriers to produce the radical species. Finally, based on the detected intermediates, we propose the degradation pathway of ILs in the plasmon-mediated process. The results of our method suggest favorable application in the treatment of wastewater.

## 1. Introduction

Ionic liquids (ILs) are organic salts comprising bulky asymmetrical cations and weakly coordinating anions. The fascinating features of ILs are that their molecular structures and physicochemical properties could be custom designed by choosing various cations, anions, and functional groups [1]. Therefore, in past decades, ILs have been used widely in chemical synthesis, catalysis, extraction, material science, pharmaceuticals, and many other applications [2]. However, with the broad utilization of ILs, specific amounts inevitably migrate into the environment through effluent emission, as many commonly used ILs are highly water soluble and chemically stable. Moreover, extensive studies have confirmed the cytotoxicity, environmental toxicity, and microbial toxicity of ILs [3–7]. This is the reason for ILs being included in the list of so-called “contaminants on the horizon” [8]. Various methods, such as biodegradation [9] and chemical oxidation [10,11] have been adopted to degrade ILs. However, owing to the high chemical stability of ILs and their strong resistance to biodegradation in nature, and the complicated process of the currently employed methods, the degradation efficiency of ILs is far from satisfactory. Consequently, it remains urgent to develop an effective and sustainable strategy to degrade ILs in various environments.

The advanced oxidation process (AOP) could be a promising route for the efficient degradation of ILs in the aquatic environment. In recent

years, AOP, based on hydroxyl ( $\cdot\text{OH}$ ) or sulfate radical ( $\text{SO}_4^{\cdot-}$ ), have been utilized widely to oxidize nocuous and refractory organic contaminants into polar and harmless compounds [12–14]. In addition, they have been mineralized into  $\text{CO}_2$  and  $\text{H}_2\text{O}$  [15–17] because of their high efficiency, simple operation, non-selectivity, and good reproducibility.

However, a weakness of  $\cdot\text{OH}$ -based AOP is that it is conducted in multistep pathways and usually requires an acidic environment. Moreover, the efficiency of  $\cdot\text{OH}$ -based AOP is severely inhibited in complex environments containing large amounts of dissolved organic matter and carbonate/bicarbonate anions, with both being the main  $\cdot\text{OH}$  scavengers [18]. In comparison, the advantages of  $\text{SO}_4^{\cdot-}$  radicals compared with  $\cdot\text{OH}$  are their longer half-life, higher standard reduction potential (2.5–3.1 V vs 1.8–2.7 V), wider tolerance of pH range [19], and higher reaction stoichiometric efficiency (RSE, i.e., the mole ratio of the probe degraded over the oxidant consumed) [20–27]. Therefore, to a certain extent,  $\text{SO}_4^{\cdot-}$ -based AOP has taken the place of the  $\cdot\text{OH}$ -based process in recent years. The most common method to the in-situ generation of  $\text{SO}_4^{\cdot-}$  is to activate persulfate (PS) by either the one-electron reduction or the homolytic cleavage of its O–O bond. These are done by inputting heat energy [28–30], ultrasonication [31], and ultraviolet (UV) light radiations [32,33]. Alternatively, by adding transition metal catalysts in homogeneous [29,34] and heterogeneous systems using iron particles [25,35,36], or incorporated iron in a new material such as metal organic framework (MOF) [26].

<sup>\*</sup> Corresponding authors.

E-mail addresses: [luweiwei@haust.edu.cn](mailto:luweiwei@haust.edu.cn) (W. Lu), [ksyao@haust.edu.cn](mailto:ksyao@haust.edu.cn) (K. Yao), [sgpeng@haust.edu.cn](mailto:sgpeng@haust.edu.cn) (S. Peng).

<https://doi.org/10.1016/j.apcatb.2021.120751>

Received 14 June 2021; Received in revised form 17 September 2021; Accepted 22 September 2021

Available online 24 September 2021

0926-3373/© 2021 Elsevier B.V. All rights reserved.

Among these methods, producing  $\text{SO}_4^-$  through light irradiation has increasingly attracted research attention [26,37–39]. On the one hand, sunlight is renewable, abundant, and facilely accessible; on the other hand, photo-activation could achieve high efficiency of organic degradation and mineralization rates with a simple operation under mild conditions. For example, Ismail et al. [37] used  $\text{TiO}_2$  as a photo-activator and UV light as inputting energy to generate  $\text{SO}_4^-$  for degrading sulfaclozine. The results have shown that this  $\text{TiO}_2/\text{K}_2\text{S}_2\text{O}_8/\text{UV}$  system has the highest elimination percentage of sulfaclozine compared with those of the  $\text{TiO}_2/\text{UV}$  and  $\text{K}_2\text{S}_2\text{O}_8/\text{UV}$  systems. This superior elimination ability is ascribed to the photo-excited charge carrier in the  $\text{TiO}_2$  photocatalyst of the  $\text{TiO}_2/\text{K}_2\text{S}_2\text{O}_8/\text{UV}$  system being captured efficiently by the electron acceptor of  $\text{K}_2\text{S}_2\text{O}_8$  for in situ producing of the  $\text{SO}_4^-$  radicals that attack the contaminants. Wang et al. [38] designed  $\text{g-C}_3\text{N}_4/\text{MnFe}_2\text{O}_4/\text{graphene}$  composite photocatalysts for photo-generation of  $\text{SO}_4^-$  from persulfate  $\text{K}_2\text{S}_2\text{O}_8$  to degrade metronidazole. The results have shown that the synergistic effect of the improved light absorption and efficient charge separation of these composite photocatalysts enhanced the generation efficiency of active  $\text{SO}_4^-$ . The enhanced generation efficiency resulted in an almost 3.5 times higher degradation rate of  $\text{g-C}_3\text{N}_4/\text{MnFe}_2\text{O}_4/\text{graphene}$  than that of  $\text{g-C}_3\text{N}_4$ . Al Asmar et al. [26] demonstrated the vital role that UVA plays in improving the degradation of naproxen in a PS activation system driven by the addition of a MOF catalyst-like material, such as MIL-88A. These selected examples have confirmed the feasibility and effectiveness of the photo-activation method in  $\text{SO}_4^-$ -based AOP for degrading various organic contaminants. However, choosing semiconductors as the photo-activator of PS leads to two main problems. First, the larger bandgap of semiconductors (e.g., 3.2 eV for anatase  $\text{TiO}_2$ ) means that activation can only be initiated under illumination by UV light. Second, the quicker recombination of photo-induced charge carriers in the semiconductor severely limits their performance in  $\text{SO}_4^-$ -based AOP [40,41]. Moreover, MOF systems are not easily synthesized in some instances and, to a certain extent, are pH and temperature dependent. Therefore, a new and efficient type of photo-activator that could be operated in the visible light region is crucial for the further development of  $\text{SO}_4^-$ -based AOP.

Plasmonic metals (mainly Ag, Au, Cu, and Al), which have localized surface plasmon resonance (SPR) in the visible light region, could be an attractive option as efficient photo-activators. The SPR, a phenomenon of group oscillation of free electrons on a metal surface, could be triggered by the periodic electromagnetic field of incoming light. The energetic charge carriers of electrons and holes could be generated immediately during the damping process of SPR, and these active carriers could be utilized to drive the chemical reactions. Compared with semiconductors, the fascinating aspects of plasmonic materials include (1) unlike semiconductors, plasmonic metals have no bandgap, and the SPR peak (i.e., the excited wavelength), as well as the energy distribution of the excited carriers, could be adjusted facilely across the entire solar spectra by controlling the composition, size, structure, and shape; (2) unlike the formation of bulk-based charge carriers in semiconductors, the energetic charge carriers in plasmonic metals are formed mainly at the surface, facilitating their participation in a chemical reaction. These unique properties have led to plasmonic metals or their composites having been applied extensively to catalyze different types of chemical reactions or induce several brand-new chemical transformations. These transformations include  $\text{H}_2$  dissociation [42,43],  $\text{O}_2$  activation [44], catalytic oxidation [45], Suzuki coupling reaction [46], and  $\text{N}=\text{N}$  bond formation [47]. However, these potential plasmonic photocatalysts have rarely been adopted as photo-activators to generate active  $\text{SO}_4^-$  radicals for degradation. In this regard, it is critical to develop this plasmon-mediated strategy to investigate the effect of the SPR of plasmonic metals on their role as photo-activators in visible light.

In the current study, inspired by the progress on  $\text{SO}_4^-$ -based AOP for degrading contaminants, as well as the advantages of plasmonic catalysis, we selected and prepared Ag@Pd core-shell nanocubes to serve as the plasmonic photo-activator in investigating the SPR-mediated process for

generating  $\text{SO}_4^-$  and its applications in degrading imidazolium-based ILs. After the Ag@Pd core-shell nanocubes were structurally characterized, their photodegradation activity for ILs degradation was investigated and compared with that of pure Ag nanocubes. The electron paramagnetic resonance (EPR) technique was used to detect the reactive species in this newly developed photo-activated AOP. Subsequently, a wavelength-dependent study was conducted to confirm the plasmon-mediated nature of the degradation method. Further, electrodynamic finite element method (FEM) simulation was performed to investigate the impact of the Pd shell on the energy dissipation pathway and the generation site of energetic charge carriers. Finally, the organic intermediates were detected and analyzed to understand the degradation mechanism of the imidazolium-based ILs in this new plasmon-mediated AOP.

## 2. Experimental

### 2.1. Chemicals and materials

Silver nitrate ( $\text{AgNO}_3$ ,  $\geq 99.8\%$ ), ethylene glycol ( $\text{C}_2\text{H}_6\text{O}$ ,  $\geq 99\%$ ), sodium sulfide nonahydrate ( $\text{Na}_2\text{S} \cdot 9\text{H}_2\text{O}$ ,  $\geq 99\%$ ), polyvinylpyrrolidone (PVP, molecular weight:  $\sim 29\,000$ ), ascorbic acid (AA,  $\text{C}_6\text{H}_8\text{O}_6$ ,  $\geq 99\%$ ), sodium hydroxide ( $\text{NaOH}$ ,  $\geq 98\%$ ), sodium tetrachloropalladate ( $\text{Na}_2\text{PdCl}_4$ ,  $\geq 98\%$ ), and potassium persulfate ( $\text{K}_2\text{S}_2\text{O}_8$ ,  $\geq 99.0\%$ ) were all purchased from Shanghai Aladdin Biochemical Technology Co. Ltd. 1-butyl-3-methylimidazolium bromide ( $[\text{C}_4\text{mim}]\text{Br}$ ,  $\geq 97\%$ ) was supplied by Shanghai Macklin Biochemical Co., Ltd.

### 2.2. Preparation of Ag and Ag@Pd nanomaterials

Ag nanocubes were prepared by the polyol method, as reported by Xia and coworkers [48], and were subsequently dispersed in water for further use. The Ag@Pd nanocubes were synthesized by the seed-mediated method [49,50], with the prepared Ag nanocubes being used as the seeds, and the  $\text{Na}_2\text{PdCl}_4$  salts, as the Pd source, were reduced on the surface of the Ag seed. First, aqueous solutions of polyvinylpyrrolidone (PVP; 50 mg, 3 mL), ascorbic acid (AA; 100 mg, 1.5 mL), and NaOH (1.25 M, 600  $\mu\text{L}$ ) were mixed, to which 0.3 mL of the stored Ag nanocube solution was added. Subsequently, an aqueous solution of  $\text{Na}_2\text{PdCl}_4$  (8.5 mg, 16 mL) was dropped into the above mixture solution at a rate of 8 mL/h by a peristaltic pump. After the reaction, the Ag@Pd nanocrystals were centrifugally washed four times at 10,000 rpm and dispersed in water.

### 2.3. Characterizations

The ultraviolet–visible (UV–vis) spectra of Ag and Ag@Pd nanocubes were recorded by ultraviolet–visible spectrophotometry (Beijing Persee Instruments Co., China). The transmission electron microscopy (TEM) and high-resolution transmission electron microscopy (HRTEM) images of the prepared catalysts were characterized by a transmission electron microscope (Titan G2 60-300, FEI Company, USA). The elements and their distribution in the samples were characterized by energy dispersive spectroscopy (EDS) mapping by a field-emission scanning transmission electron microscope (Hitachi HD-2300A; Hitachi Ltd., Japan), equipped with an energy dispersive X-ray spectrometer at an accelerating voltage of 200 kV. Inductively coupled plasma-atomic emission spectrometry (ICP-AES) analysis was performed with a Shimadzu ICPE-9820 apparatus (Shimadzu Corporation, Japan) to quantify the Ag and Pd components of the hybrid catalysts. X-ray photoelectron spectroscopy (XPS) data were taken on a Thermo ESCALAB 250Xi (Thermo Fisher Scientific, USA), using Al  $\text{K}\alpha$  radiation (1486.6 eV) as the radiation source. Powder X-ray diffraction (XRD) patterns were collected on an X-ray diffractometer (Bruker D8 Advance; Bruker Scientific Instruments, USA), with Cu  $\text{K}\alpha$  radiation ( $\lambda = 1.5406\text{ \AA}$ ) at a scan rate of  $5^\circ/\text{min}$  from  $30^\circ$  to  $90^\circ$ . The Electrochemical Impedance Spectroscopy (EIS) was measured on an electrochemical workstation (CHI 660E, CH Instruments Inc., USA) in a

three-electrode system under light illumination, in which an A 300 W Xe lamp (CEAULIGHT, CEL-HXF-UV 300), equipped with an AM1.5 light filter, was used to simulate sunlight irradiation conditions.

The EPR spectra were measured on a spectrometer (Bruker, A300; USA) equipped with a cylindrical resonator at a microwave frequency of approximately 9.852 GHz (X-band). We used 5, 5-dimethylpyrroline oxide (DMPO) to capture  $\text{SO}_4^{\cdot-}$ ,  $\cdot\text{OH}$ , and  $\text{O}_2^{\cdot-}$  radicals, with the trapping agent for  $^1\text{O}_2$  being 2, 2, 6, 6-tetramethyl-4-piperidine (TEMP). The tested supernatant (80  $\mu\text{L}$ ) was poured into a microcapillary tube, with acquisition time of 60 min required to identify the reactive species produced in the plasmon-mediated process. The settings of the EPR spectrometer were as follows: center field 351 mT, sweep width 10 mT, sweep time 61.44 s, modulation amplitude 0.1 mT, modulation frequency 100 kHz, and microwave power attenuation 10 dB.

#### 2.4. Photodegradation of ILs

The IL degradation experiments were conducted in a cylindrical reactor, with the reaction temperature being controlled by circulating the water through the outer jacket of the reactor. The illumination light, with wavelengths of 365 nm, 420 nm, 520 nm, 605 nm, and 730 nm, was supplied by a light-emitting diode light source (PLS-LED100, Beijing Perfectlight Technology Co., Ltd., China). Typically, an aqueous solution (100 mL), containing IL (0.1 mM),  $\text{K}_2\text{S}_2\text{O}_8$  (10 mM) and plasmonic Ag@Pd catalysts (0.7 g/L), was stirred under the dark condition at 25 °C for 15 min. Subsequently, the reaction was initiated by light illumination. Afterward, 0.5 mL of the reaction solution was taken out at an interval of 1 h to quantitatively measure the concentration of remaining ILs by UV-vis spectrophotometry according to the Beer-Lambert law. The degradation degree is calculated as follows (Eq. 1):

$$\text{Degradation degree (\%)} = \left(1 - \frac{C_t}{C_0}\right) \times 100 \quad (1)$$

where  $C_0$  and  $C_t$  refer to the initial concentration of IL and the concentration of IL at the photodegradation time  $t$ , respectively.

The RSE, defined as the number of moles of probe degraded ( $n(\text{ILs})_{\text{degraded}}$ ) over the number of moles of PS consumed ( $n(\text{PS})_{\text{consumed}}$ ), is calculated as follows (Eq. 2):

$$\text{RSE (\%)} = \frac{n(\text{ILs})_{\text{degraded}}}{n(\text{PS})_{\text{consumed}}} \times 100 \quad (2)$$

The quantity of PS was determined according to an high performance liquid chromatography (HPLC) method developed by Ghauch and co-workers [21].

The possible intermediates in the degradation course were determined by a gas chromatograph (GC, Trace 3000)-single quadrupole mass spectrometer (MS, ISQ 7000; Thermo Fisher Scientific, USA) equipped with a capillary column (TG-624SilMS, 30 m  $\times$  0.25 mm  $\times$  1.40  $\mu\text{m}$ ).

#### 2.5. FEM calculation

The optical property Ag@Pd was simulated by the finite element method. Core-shell nanocubes with an Ag core edge length of 45 nm and a Pd shell of 1.7 nm were constructed, and the wavelength range from 300 nm to 600 nm was calculated. The nanocubes in the simulations were smoothed with a 5 nm round corner to reflect the particle shape observed in TEM images. The dielectric functions of silver and palladium were obtained by Lorentz-Drude dispersion model to fit the experimental data in the book of Palik [51].

### 3. Results and discussion

#### 3.1. Characterization and formation mechanism of Ag@Pd

The Ag nanocubes and Ag@Pd core-shell nanocubes were prepared by the polyol method and seed-mediated method, respectively. The SEM image in Fig. S1 shows that the prepared Ag nanocubes have an average side length of 45 nm. These prepared Ag nanocubes were used as seeds and  $\text{Na}_2\text{PdCl}_4$  as the Pd source to prepare Ag@Pd core-shell nanocubes [50,52,53]. In Ag@Pd synthesis, with the slow drop of  $\text{Na}_2\text{PdCl}_4$  solution into the reaction solution containing Ag nanocubes, AA, and NaOH, the solution gradually changed from light yellow to brown, indicating the reduction of  $\text{Pd}^{2+}$  onto the surface of Ag nanocubes. To confirm this occurrence, the structure of the prepared bimetallic Ag@Pd samples was characterized, with the results shown in Fig. 1. The TEM image in Fig. 1a shows that the prepared Ag@Pd nanocrystals still maintain the cubic shape of the Ag core. The HRTEM image of a representative Ag@Pd nanocube in Fig. 1b shows that the formed Pd shell is ultra-thin, with thickness of approximately only 1.7 nm. To further investigate the elemental distribution of the sample, the EDS mapping of the elements Ag, Pd, and their overlay for a single Ag@Pd nanocube (see Fig. 1c) are shown in Fig. 1d-f, respectively. These element mappings clearly show the uniform distribution of metallic Pd atoms on the surface of the Ag nanocube. The color changes of the Ag and Ag@Pd sample solutions can be reflected by their UV-vis spectra (see Fig. 1g). The UV-vis curve of Ag nanocubes has a strong dipole SPR peak at 420 nm and a characteristic quadrupole shoulder at 365 nm. When the Ag@Pd core-shell structure is formed, the UV-vis spectrum is broadened, and the plasmonic peak is slightly blue-shifted.

To improve our understanding of the structure and surface properties of the Ag@Pd samples, we conducted XPS and XRD characterization. The obtained XPS results are shown in Fig. S2. All the signals in the scan survey spectra of Fig. S2a could be assigned to Ag, Pd, C, N, and O elements. The appearance of the C, N, and O peaks could result from the PVP used as the capping agent. The high-resolution spectra for Ag 3d and Pd 3d orbitals are shown in Fig. S2b and c, respectively. As shown by Fig. S2b, there are two peaks at binding energy (BE) values of 368.2 and 374.1 eV, which could be assigned to the  $3d_{5/2}$  and  $3d_{3/2}$  state of metallic Ag [54], respectively. The two peaks at BE values of 335.0 and 340.3 eV in Fig. S2c are related to the  $3d_{5/2}$  and Pd  $3d_{3/2}$  states of metallic Pd, respectively [54]. The XPS characterization, therefore, confirms that Ag and Pd are metallic for the prepared core-shell Ag@Pd nanocubes.

Subsequently, XRD analysis of Ag and Ag@Pd was performed, with the results shown in Fig. S3a and b, respectively. The standard card of Ag (Fig. S3c) and Pd (Fig. S3d) are included for indexing of the diffraction peaks. The observed peaks at  $38.2^\circ$ ,  $44.4^\circ$ ,  $64.3^\circ$ ,  $77.5^\circ$ , and  $81.4^\circ$  in the diffraction curves of Ag (Fig. S3a) correspond to (111), (200), (220), (311), and (222) planes of the typical face-centered cubic structure of Ag. After coating Pd metal onto Ag nanocubes and forming an Ag@Pd core-shell structure (Fig. S3b), the independent peaks of the Pd shells could not be indexed directly. However, there is an apparent shoulder at the right side of each Ag diffraction peak. After deconvolution, the diffraction peaks of Pd (the red color) and Ag (the blue color) could be distinguished.

In the preparation of core-shell-type metal-metal composite nanomaterials, a key action is suppressing the galvanic reaction between the core metal and the added salt that contains the shell element. We used AA as a reductant to inhibit the galvanic reaction between Ag and  $\text{Na}_2\text{PdCl}_4$ . As the existing form of AA and, therefore, its reduction potential, is significantly dependent on the pH value of the solution [55], a higher pH value is required to increase its reduction capacity. In this



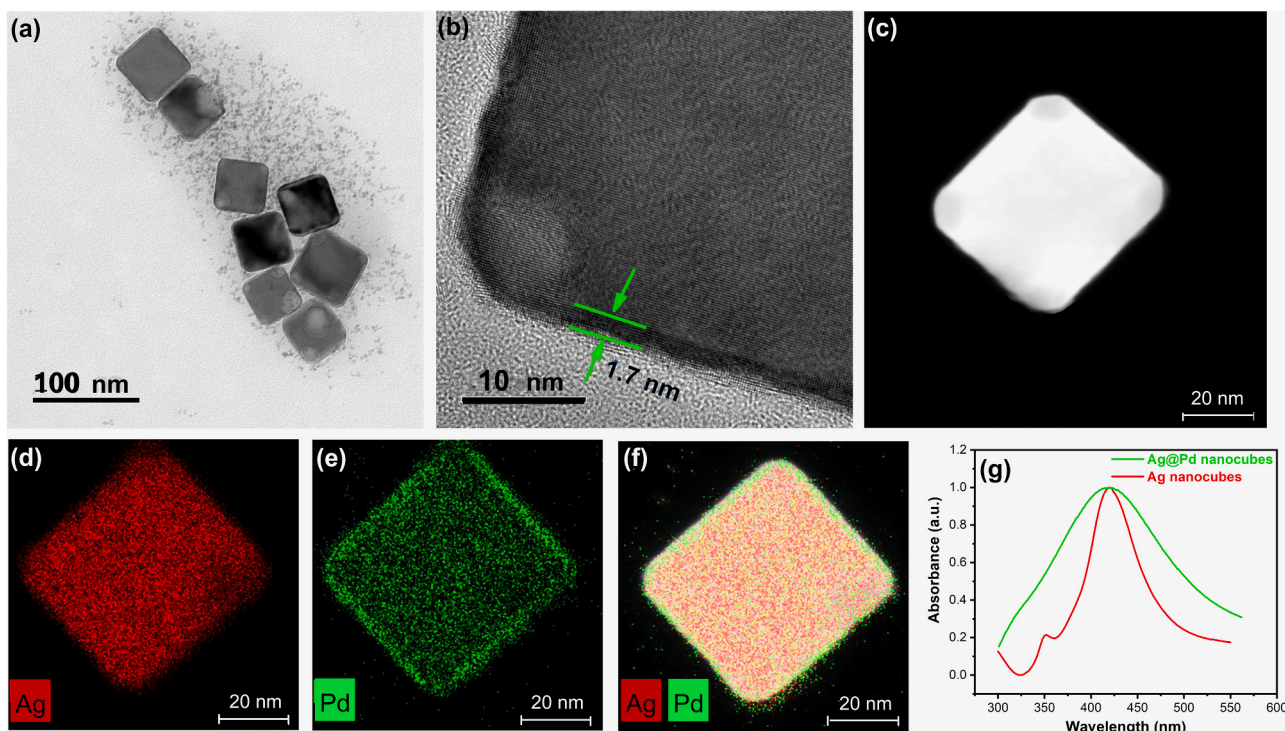


Fig. 1. Characterization of the as-prepared Ag@Pd core-shell nanocubes. (a) TEM image, (b) HRTEM image, (c) STEM-HAADF image of a typical Ag@Pd nanocube; STEM-EDS element mapping of Ag (d), Pd (e), and their overlaid mapping (f); UV-vis spectra of the prepared Ag and Ag@Pd nanocubes (g).

study, the pH value was 12.1 when an aqueous solution (600  $\mu$ L) of NaOH (1.25 M) was added. The relatively higher pH value implied that the main existing species of AA is diascorbate ( $\text{Asc}^{2-}$ ), which is an extremely strong reductant [55]. Therefore, the  $\text{Pd}^{2+}$  would be reduced preferentially by  $\text{Asc}^{2-}$  when  $\text{Na}_2\text{PdCl}_4$  is added to the mixture solution of Ag nanocubes and  $\text{Asc}^{2-}$ , as  $\text{Asc}^{2-}$  has higher reduction capacity compared with that of Ag metal. In contrast, without the addition of NaOH, a rattle structure with the void between the shell of Pd and the core of Ag would be formed (see Fig. S4).

### 3.2. Performance of Ag and Ag@Pd for photodegradation of ILs

After the structural characterization of Ag and Ag@Pd, we investigated their activities for photodegradation of ILs. The ILs of [C<sub>4</sub>mim]Br were selected as the representative, as they are the most popular imidazole-based ILs because of their higher stability and water solubility. Moreover, the toxicity of [C<sub>4</sub>mim]Br has been investigated and verified [56]. The degradation performance of Ag@Pd was evaluated by monitoring the concentration of [C<sub>4</sub>mim]Br at a fixed interval of 1 h by UV-vis absorption spectra (see Fig. S5). Fig. 2a shows the degradation curves of Ag and Ag@Pd under light irradiation and dark conditions. As a control, the degradation of ILs with light illumination but without adding Ag and Ag@Pd was tested, and the results obtained (see Fig. 2a) show that [C<sub>4</sub>mim]Br could not be degraded in an  $\text{K}_2\text{S}_2\text{O}_8$ /light system. This failed photodegradation could be ascribed to the photon energy of 420 nm visible light being too low to break the O-O bond of persulfate to generate the active radical species. Moreover, as shown by Fig. 2a, neither Ag nor Ag@Pd show degradation activities for IL under dark conditions. With light illumination, the degradation percentages of IL for Ag and Ag@Pd after 12 h were 38.13% and 74.21%, respectively. The Ag@Pd core-shell nanocubes have much higher photodegradation activity than do pure Ag nanocubes, indicating the promotional effect of the non-plasmonic Pd shell on the plasmonic Ag core under light illumination. In addition, compared with popular semiconductors, g-C<sub>3</sub>N<sub>4</sub> and P25 TiO<sub>2</sub> (Degussa), Ag@Pd show higher photodegradation activity

under light irradiation (300 W Xe lamp with AM1.5 light filter), verifying the high efficiency of this Ag@Pd/ $\text{K}_2\text{S}_2\text{O}_8$ /vis system (see Fig. S6).

As the stability and reusability of catalysts are essential parameters for their applications, we subsequently evaluated the stability and reusability of the catalyst of Ag@Pd by employing cyclic experiments. After each run of catalytic degradation, the Ag@Pd catalysts were isolated from the reaction solution by centrifugation. Subsequently, the isolated catalysts were re-dispersed into the new degradation solution to evaluate their remaining degradation activity. The obtained degradation curves of the five successive runs are shown in Fig. S7. The figure shows that after five cycles the degradation degree of ILs for the Ag@Pd catalyst decreased only slightly from 74.21% to 66.86%, maintaining 90.1% of the degradation activity. These cyclic experiments have, therefore, proven the high stability and good reusability of the prepared Ag@Pd catalysts.

Another concern is the leaching of catalysts in the application of the Ag@Pd photocatalyst. To determine whether catalyst leaching occurred during the degradation, the Ag@Pd catalysts were centrifuged from the reaction solution after the degradation reaction. Afterward, the contents of Ag and Pd in the sediment, as well as in the supernatant, were determined by ICP-AES. As indicated in Table S1, the Ag and Pd content of the Ag@Pd catalysts show almost no changes after the degradation reaction, and Ag and Pd are not detected in the supernatant. These results have proven that catalyst leaching does not occur for Ag@Pd, probably because the high chemical stability of the Pd shell prevents the corrosion of the catalysts.

In addition, we calculated the RSE (RSE%), as a useful indicator of the radical-based AOP [21,27,29,30], at 19.2% and 28.7% for Ag and Ag@Pd, respectively, which further verified the higher activity of Ag@Pd catalysts. However, compared with results obtained previously [22,24,26,27], our results for the RSE% of Ag@Pd catalysts are not at the top level (see Table S2), which could be ascribed probably to the different method of activating PS for the generation of  $\text{SO}_4^{\cdot-}$  radicals.

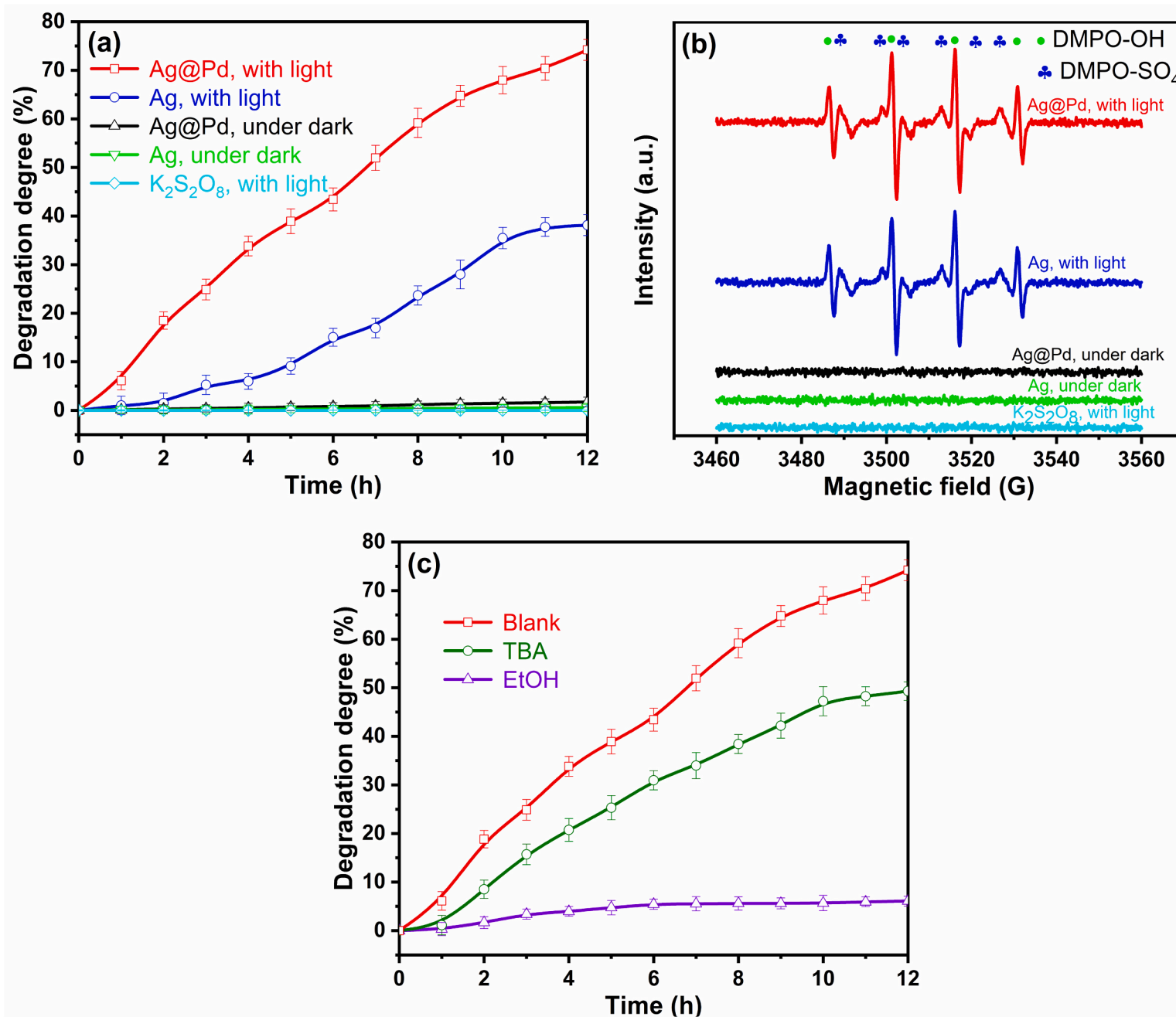


**Fig. 2.** (a) Performance of Ag and Ag@Pd for [C<sub>4</sub>mim]Br degradation under dark conditions or with light illumination (light wavelength 420 nm, light intensity 220 mW/cm<sup>2</sup>); (b) EPR spectra of Ag/K<sub>2</sub>S<sub>2</sub>O<sub>8</sub> and Ag@Pd/K<sub>2</sub>S<sub>2</sub>O<sub>8</sub> systems under dark conditions or with light illumination; (c) Addition of radical scavengers to the degradation degree of [C<sub>4</sub>mim]Br in the Ag@Pd/PS/vis system. The error bar means  $\pm 1$  standard error calculated from three independent experiments.

### 3.3. Determination of the active radical species

It is accepted that for the AOP the generated radicals of  $\text{SO}_4^{\cdot-}$  and  $\cdot\text{OH}$  are the main active species to attack and degrade the contaminants [57, 58]. To determine the active species in the plasmon-mediated photodegradation system in our study, we carried out EPR measurements. We used DMPO, a classical spin-trapping agent to capture the active radicals for EPR measurement. As the EPR spectra in Fig. 2b show, regardless of whether the catalyst is Ag or Ag@Pd, intense signals of both DMPO-OH and DMPO- $\text{SO}_4^{\cdot-}$  are detected, indicating that two types of free radicals of  $\text{SO}_4^{\cdot-}$  and  $\cdot\text{OH}$  are generated in this SPR-mediated degradation process, and they are responsible for the degradation of ILs.

After verification of the active radical species of  $\cdot\text{OH}$  and  $\text{SO}_4^{\cdot-}$ , their contributions in the overall degradation process were determined further by using tertbutyl alcohol (TBA) and ethanol (EtOH) as the scavengers [40,57,59–62]. In addition, to ensure the preferential reaction between radicals and scavengers, an excessive number of scavengers (5 M, 50,000 times over the concentration of [C<sub>4</sub>mim]Br) was added to the reaction solution [60,62,63]. As shown in Fig. 2c, the degradation degree of [C<sub>4</sub>mim]Br in the presence of Ag@Pd decreased from 74.21% to 49.25% and 6.03% with the addition of TBA and EtOH after 12 h, respectively. This result has confirmed that this plasmon-mediated degradation process is a radical-based oxidation process, which agrees with the above EPR investigation. As EtOH could scavenge both  $\text{SO}_4^{\cdot-}$  and  $\cdot\text{OH}$ , their quenching accounts for a decrease of 68.18% (from 74.21% to 6.03%) in the degree of degradation after 12 h of reaction. When TBA, a preferential scavenger of  $\cdot\text{OH}$ , was used, a decrease of 24.96% (from 74.21% to 49.25%) in the degree of degradation was observed. Therefore, we concluded that quenching of  $\cdot\text{OH}$  and  $\text{SO}_4^{\cdot-}$  accounted for a decrease of 24.96% and 43.22% in the degree of degradation, respectively. Our results have confirmed that the effect of  $\text{SO}_4^{\cdot-}$  was more significant than that of  $\cdot\text{OH}$  in this photodegradation process. It should be noted here, as shown in Fig. 2c, that after adding ethanol as the quencher of  $\cdot\text{OH}$  and  $\text{SO}_4^{\cdot-}$ , the degradation percentage first increases slightly and then remains almost unchanged. To confirm the existence of other active species besides  $\cdot\text{OH}$  and  $\text{SO}_4^{\cdot-}$ , we performed EPR analysis of other popular reactive oxygen species of  $\text{O}_2^{\cdot-}$  and  $^1\text{O}_2$ , but neither was detected. Moreover, the unchanged degradation percentage at the latter stage probably excluded the possibility of other reactive species existing in this Ag@Pd/PS/vis system, as photodegradation would proceed continually in the presence of reactive species other than  $\text{SO}_4^{\cdot-}$  and  $\cdot\text{OH}$  that would account for the degradation. Therefore, the occurrence of degradation after the addition of ethanol could be ascribed to the generated overall reactive radicals not

being trapped promptly when the radical quenchers were added and, therefore, they were still playing a role in the initial degradation stage [64–67].

### 3.4. Effect of light wavelength on the degradation performance

A unique characteristic of plasmonic photocatalysts is their wavelength-dependent performance [68–70], as each plasmonic metal has its own specific SPR fingerprint. In addition, the wavelength of illumination light determines the energy of the incident photon and, consequently, the energy distribution of the plasmon-generated electrons and holes. Therefore, to verify that the generation of active radicals and the subsequent photodegradation of ILs in the presence of Ag@Pd was, indeed, a plasmon-mediated process, their degradation activity was tested under illumination light with different wavelengths. The results shown in Fig. 3a indicate that among the four tested wavelengths in the visible light region, the illumination near the SPR peak of Ag@Pd at a wavelength of 420 nm (see Fig. 1g) brings about the highest degradation activity. This wavelength-dependent performance of Ag@Pd photocatalysts provides strong evidence of their plasmon-driven nature for the  $\text{SO}_4^{\cdot-}$ -based degradation process. This point can also be corroborated by the intensity of the EPR signal measured under light with different wavelengths (see Fig. 3b). The signals of  $\text{SO}_4^{\cdot-}$  and  $\cdot\text{OH}$  radicals gradually weaken with an increase in the optical wavelength used, which is roughly consistent with the degradation profile under light with different wavelengths in Fig. 3a [63]. It should be noted here that the illumination of UV light at 365 nm provides comparative degradation activity compared with that of visible light of 420 nm, although the UV light could not produce the occurrence of SPR for Ag@Pd nanocubes (see Fig. 1g). However, UV light could induce interband electronic excitation to generate energetic electrons and holes [71,72], resulting in the formation of active  $\text{SO}_4^{\cdot-}$  radicals. In addition, the high energy of UV light could directly activate the  $\text{K}_2\text{S}_2\text{O}_8$  to produce the  $\text{SO}_4^{\cdot-}$  radicals [32,33,40], which could also account for the high activity under UV light.

### 3.5. Effect of optical power density on the degradation of [C<sub>4</sub>mim]Br

We also studied the effect of light power density on the degradation performance of the Ag@Pd photocatalyst. Fig. 4 shows the degradation profile of Ag@Pd under light illumination of 420 nm, but with different intensities of light. The figure shows that the degradation rate is nearly proportional to the intensity of the light illumination. This result was

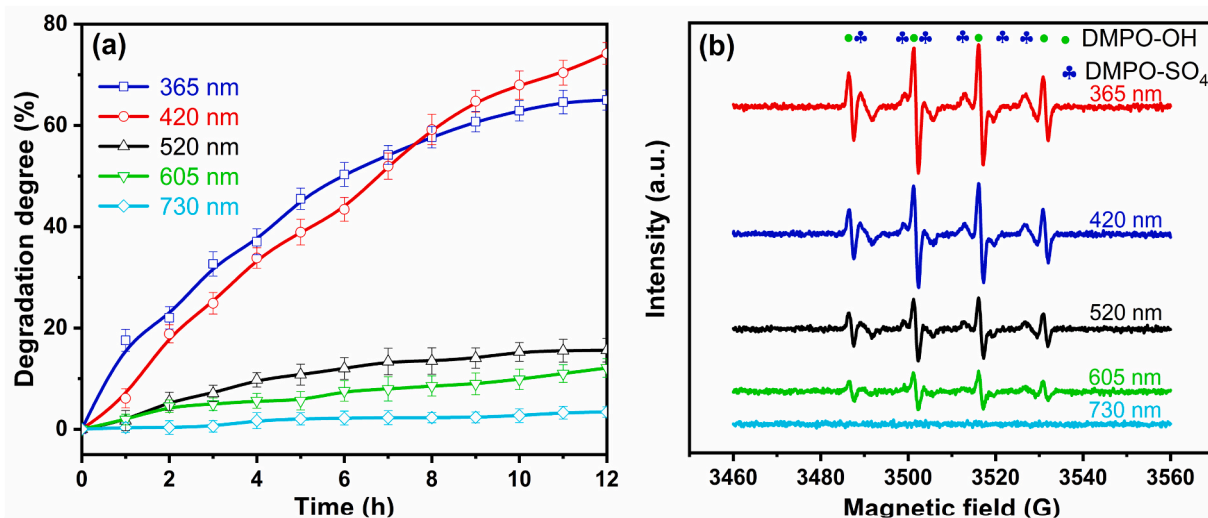


Fig. 3. Degradation degree of [C<sub>4</sub>mim]Br as a function of time (a) and the EPR spectra (b) in the Ag@Pd/K<sub>2</sub>S<sub>2</sub>O<sub>8</sub> system under light illumination, with wavelengths of 365, 420, 520, 605, or 730 nm. The error bar means  $\pm 1$  standard error calculated from three independent experiments.



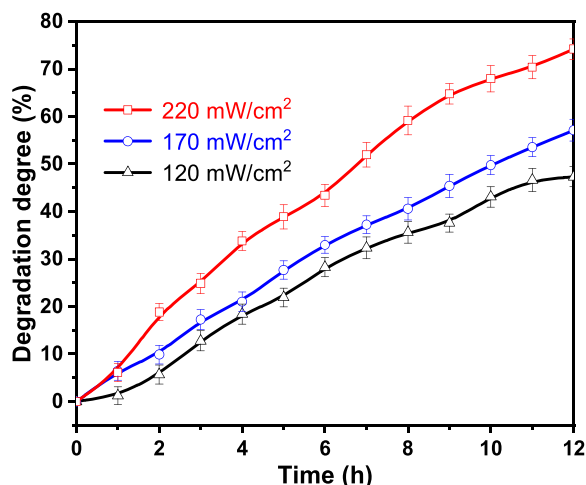


Fig. 4. Influence of light intensity on the degradation performance of Ag@Pd plasmonic photocatalyst. The error bar means  $\pm 1$  standard error calculated from three independent experiments.

consistent with expectations, as higher illumination intensity causes more incoming photons and more-energetic charge carriers, ultimately resulting in a higher rate of degradation.

### 3.6. Calculation of the plasmon property of Ag@Pd nanocubes

After verifying the plasmon-mediated nature of Ag@Pd for the efficient generation of active  $\text{SO}_4^{\cdot -}$  radicals under light illumination, we

investigated the reason for the superior performance of the Ag@Pd compared with that of pure Ag by calculating their optical properties through FEM simulations. As the absorption of photons for plasmonic catalysts determines the formation of energetic charge carriers and, ultimately, the generation of active radicals, the absorption fraction of the metallic core and shell as a function of wavelength were calculated separately. For facile comparison, we calculated the absorption fraction of the Ag core and Ag shell of the Ag@Ag nanocube (see Fig. 5a) with the same dimensions as the Ag@Pd. As shown in Fig. 5a and b, replacing the Ag shell with a Pd shell significantly enhances the absorption fraction of the outer shell. This implies that the absorption of light and the immediate creation of energetic electrons and holes occurred mainly in the outer Pd shell of the Ag@Pd nanocubes. In other words, for the bicomponent Ag@Pd core-shell nanocubes, the Pd shell offers a more convenient dissipation path for the absorbed light energy. To confirm this point, the local heating power density that denotes the generation rate of charge carriers was calculated, and the resulting maps for Ag@Ag and Ag@Pd are shown in Fig. 5c and d, respectively. As the two maps show, a bright and luminous belt is formed on the surface of the Pd shell, implying that these sites are the preferential place to dissipate the light energy into high-energy carriers. The phenomenon of flowing plasmonic energy into shell materials has been observed previously in Ag@Pt [49] and Ag@Cu<sub>2</sub>O [73] multicomponent systems by Linic and coworkers. The phenomenon has been ascribed to the higher imaginary part of the dielectric function of the shell non-plasmonic materials in comparison with the core plasmonic material. Accordingly, we believe that, for bimetallic Ag@Pd nanocubes, energetic hot carriers could be created more efficiently at the outer Pd shell under the SPR condition, resulting in the substantially increased formation of active  $\text{SO}_4^{\cdot -}$  radicals and, ultimately, the superior degradation performance of Ag@Pd compared

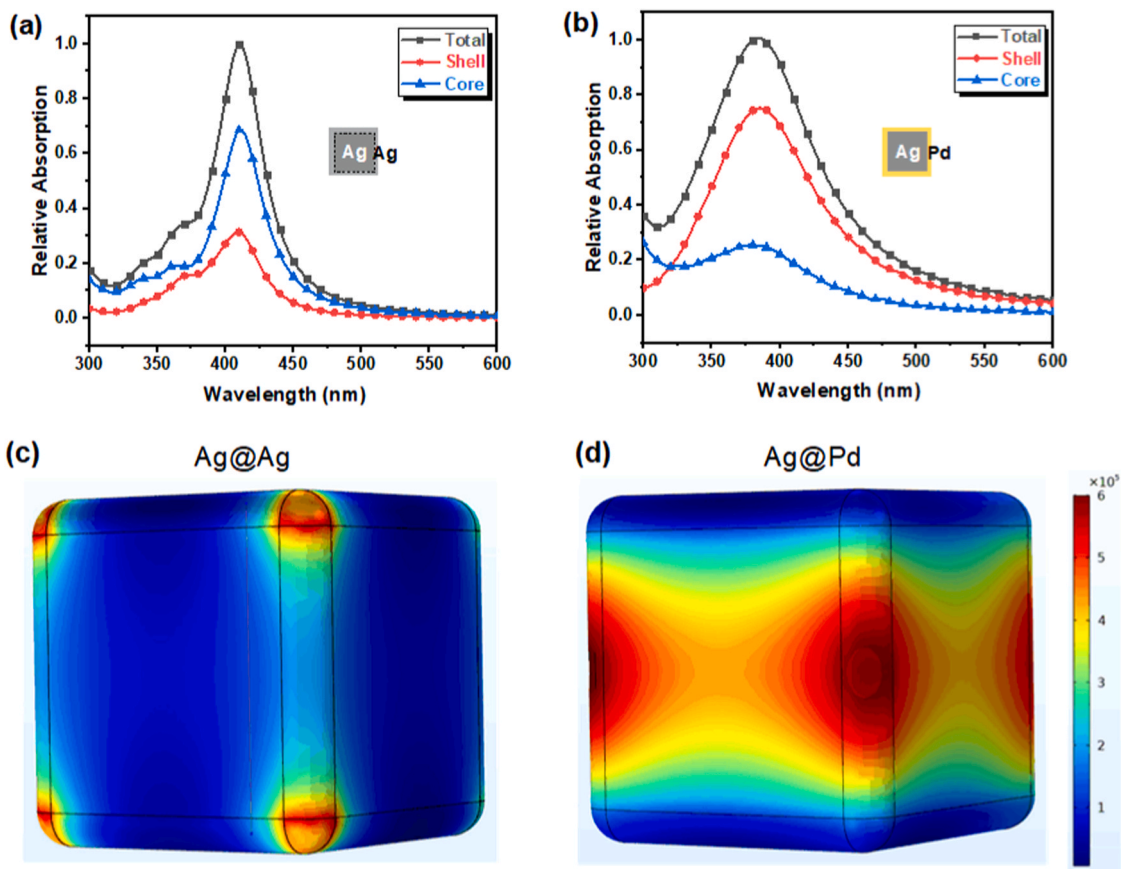


Fig. 5. Relative absorption of the core and shell of the Ag@Ag (a) and Ag@Pd (b); FEM mapping of the local heating power densities of Ag@Ag (c) and Ag@Pd (d) nanocubes.

with that of pure Ag (see Fig. 2). Furthermore, the EIS diagram in Fig. S8 shows that the radius of the semicircle is reduced substantially when Pd shells are coated onto Ag nanocubes, confirming the increased charge transfer of Ag@Pd compared with that of Ag.

### 3.7. Degradation pathway of ILs in the SRP-mediated AOP

To clarify the degradation pathway of [C<sub>4</sub>mim]Br in this plasmon-mediated AOP, the intermediate species were identified by gas chromatography/mass spectrometry (GC-MS) analysis. Owing to the low concentration and short lifetime of some degradation intermediates, it is difficult to identify them under normal degradation conditions. Therefore, higher initial concentrations of [C<sub>4</sub>mim]Br (1 mM), oxidant of K<sub>2</sub>S<sub>2</sub>O<sub>8</sub> (100 mM), and catalyst of Ag@Pd (1.40 g/L) were used. Several of the degradation products could be observed in the GC-MS detection, and further MS analysis identified certain formed intermediates (Figs. S9–15). Seven main degradation intermediates (see Fig. 6) were captured for the degradation of [C<sub>4</sub>mim]Br. These are 1-butyl-3-methyl-2,4,5-trioximidazolidine (a), N-formyl-N-methylformamide (b), N-butylformamide (c), formamide (d), butanol (e), butanoic acid (f), and acetic acid (g).

Based on the above analyses, the degradation pathway of [C<sub>4</sub>mim]Br in this plasmon-mediated oxidation process was suggested and is shown in Fig. 6 [74–76]. The first primary product is 1-butyl-3-methyl-2,4,5-trioximidazolidine (a), which is formed by the oxidation of the C atoms at 2, 4, and 5 positions of the cation [C<sub>4</sub>mim]<sup>+</sup>. This result implied that the oxidation first occurred in the imidazole ring rather than in the alkyl side chains [77]. Subsequently, the N1-C2 and C4-C5 bonds were cleaved, leading to the opening of the imidazole rings and the generation of degradation products (b) and (c) [2]. Finally, further oxidation of (c) resulted in its bond cleavage and the formation of degradation products of d, e, f, and g [74,75,78].

### 3.8. Degradation mechanism of [C<sub>4</sub>mim]Br in Ag@Pd/K<sub>2</sub>S<sub>2</sub>O<sub>8</sub>/vis system

Based on the above results, we proposed a plausible mechanism for the degradation of [C<sub>4</sub>mim]Br in the Ag@Pd/K<sub>2</sub>S<sub>2</sub>O<sub>8</sub>/vis system (see Fig. 7). In previous degradation curves and EPR results (see Fig. 2), the Ag@Pd nanocubes showed no degradation activity and no corresponding radical signal was observed under dark conditions. However, the Ag@Pd nanocubes showed apparent degradation activity and the SO<sub>4</sub><sup>•−</sup> and •OH signals were detected with light illumination. Moreover, the photodegradation performance of Ag@Pd nanocubes displayed a high dependence on the wavelength and intensity of illumination light (see Figs. 3 and 4). Therefore, we concluded that the mechanism for plasmon-mediated photodegradation of [C<sub>4</sub>mim]Br in the presence of Ag@Pd and K<sub>2</sub>S<sub>2</sub>O<sub>8</sub> could be described as follows. First, the energetic charge carriers of electrons and holes were produced efficiently at the surface of plasmonic Ag@Pd nanocubes in the damping course of their

SPR. Subsequently, the energetic electrons could efficiently activate K<sub>2</sub>S<sub>2</sub>O<sub>8</sub> and then H<sub>2</sub>O to generate highly active radicals of SO<sub>4</sub><sup>•−</sup> and •OH according to the reactions in Eqs. 3–5. Afterward, these highly active radicals were further attacked the imidazolium ring of [C<sub>4</sub>mim]Br and, finally, transformed it into degradation products with low molecular weight [40]. Moreover, Ag@Pd catalysts have a much higher ability than Ag to generate energetic charge carriers (Fig. 5), and higher degradation activity (Fig. 2), which further support our proposed plasmon-mediated degradation mechanism. Meanwhile, during the photodegradation process, the SPR-generated holes participate in oxidizing H<sub>2</sub>O to O<sub>2</sub> (Eq. 6, see detection methods of O<sub>2</sub> and the GC results in Fig. S16).



It should be noted here that K<sub>2</sub>S<sub>2</sub>O<sub>8</sub> has an important role in the plasmon-mediated degradation process because, as an efficient electron acceptor, it could facilitate capture the plasmon-induced electrons to produce SO<sub>4</sub><sup>•−</sup> free radicals. In this way, it effectively prevented electrons and holes combining and, ultimately, enhanced the degradation performance of Ag@Pd nanocubes. Further, the generated SO<sub>4</sub><sup>•−</sup> radicals could carry out the radical interconversion reactions to yield •OH radicals, another active radical species in this AOP [79].

## 4. Conclusion

Our results showed the efficiency of our proposed strategy to eliminate degradation-resistant ILs through a plasmon-mediated radical-based AOP. In addition, our method is more environmentally friendly than conventional methods. We were able to degrade more than 74.21% of a representative IL [C<sub>4</sub>mim]Br in the Ag@Pd/K<sub>2</sub>S<sub>2</sub>O<sub>8</sub>/vis system within 12 h, with irradiation from a 420 nm light. The radicals of SO<sub>4</sub><sup>•−</sup> and •OH generated from the reaction between the energetic charge carriers and the oxidant K<sub>2</sub>S<sub>2</sub>O<sub>8</sub> played a vital role in degrading [C<sub>4</sub>mim]Br. For plasmonic Ag@Pd catalysts, the Pd shell provided a facile way to dissipate the photo-energy and, subsequently, generated the energetic carriers, which accounted for their higher activity compared with that of pure Ag nanocubes. In this plasmon-mediated AOP, the imidazolium rings of ILs were initially oxidized and then opened to form some small molecules. We believe that our new plasmon-mediated photo-activation method can attract considerable interest in the field of environmental pollution control. Moreover, our method can be explored for the removal of other noxious pollutants.

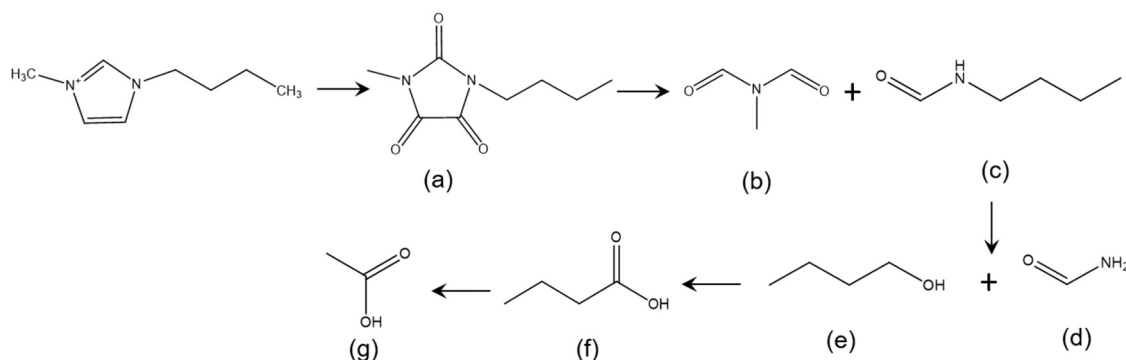


Fig. 6. Proposed degradation pathway of [C<sub>4</sub>mim]Br during plasmon-mediated SO<sub>4</sub><sup>•−</sup>-based AOP.



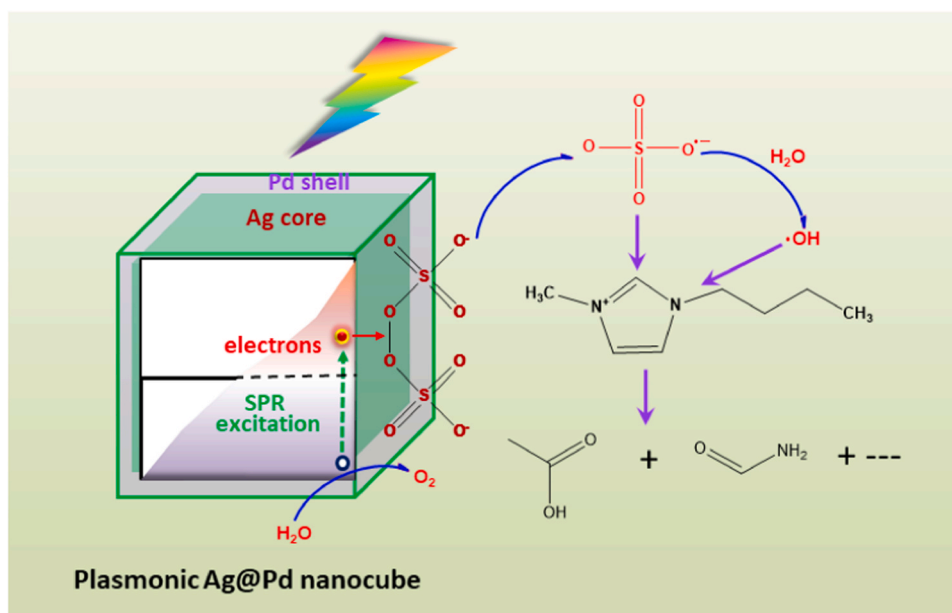


Fig. 7. Proposed mechanism for plasmon-mediated photodegradation of [C<sub>4</sub>mim]Br in the presence of Ag@Pd and K<sub>2</sub>S<sub>2</sub>O<sub>8</sub>.

#### CRediT authorship contribution statement

**Li Zhang:** Methodology, Data curation, Formal analysis, Writing – original draft, Writing – review & editing. **Weiwei Lu:** Conceptualization, Project administration, Funding acquisition, Formal analysis, Writing – original draft, Writing – review & editing. **Peng Xu:** Methodology, Data curation, Writing – review & editing. **Hao Wang:** Methodology, Writing – review & editing. **Xuefeng Wei:** Resources, Writing – review & editing. **Kaisheng Yao:** Conceptualization, Project administration, Resources, Writing – review & editing. **Shuge Peng:** Funding acquisition, Resources, Writing – review & editing.

#### Declaration of Competing Interest

The authors declare that they have no known competing financial interests or personal relationships that could have appeared to influence the work reported in this paper.

#### Acknowledgements

This work was supported by the National Natural Science Foundation of China (Grant Nos. 21673067 and 22175057).

#### Appendix A. Supporting information

Supplementary data associated with this article can be found in the online version at [doi:10.1016/j.apcatb.2021.120751](https://doi.org/10.1016/j.apcatb.2021.120751).

#### References

- [1] K. Dong, X.M. Liu, H.F. Dong, X.P. Zhang, S.J. Zhang, Multiscale studies on ionic liquids, *Chem. Rev.* 117 (2017) 6636–6695, <https://doi.org/10.1021/acs.chemrev.6b00776>.
- [2] J. Gao, L. Chen, Y.Y. He, Z.C. Yan, X.J. Zheng, Degradation of imidazolium-based ionic liquids in aqueous solution using plasma electrolysis, *J. Hazard. Mater.* 265 (2014) 261–270, <https://doi.org/10.1016/j.jhazmat.2013.11.060>.
- [3] K.S. Egorova, V.P. Ananikov, Toxicity of ionic liquids: eco(cyto)activity as complicated, but unavoidable parameter for task-specific optimization, *ChemSusChem* 7 (2014) 336–360, <https://doi.org/10.1002/cssc.201300459>.
- [4] M.C. Bubalo, K. Radosevic, I.R. Redovnikovic, J. Halambek, V.G. Srcek, A brief overview of the potential environmental hazards of ionic liquids, *Ecotox. Environ. Safe.* 99 (2014) 1–12, <https://doi.org/10.1016/j.ecoenv.2013.10.019>.
- [5] S.P.M. Ventura, A.M.M. Goncalves, T. Sintra, J.L. Pereira, F. Goncalves, J.A. P. Coutinho, Designing ionic liquids: the chemical structure role in the toxicity, *Ecotoxicology* 22 (2013) 1–12, <https://doi.org/10.1007/s10646-012-0997-x>.
- [6] I.F. Mena, E. Diaz, J. Palomar, J.J. Rodriguez, A.F. Mohedano, Cation and anion effect on the biodegradability and toxicity of imidazolium- and choline-based ionic liquids, *Chemosphere* 240 (2020), 124947, <https://doi.org/10.1016/j.chemosphere.2019.124947>.
- [7] S. Ostadjo, P. Berton, J.L. Shamshina, R.D. Rogers, Scaling-up ionic liquid-based technologies: how much do we care about their toxicity? prima facie information on 1-ethyl-3-methylimidazolium acetate, *Toxicol. Sci.* 161 (2018) 249–265, <https://doi.org/10.1093/toxsci/kfx172>.
- [8] S.D. Richardson, T.A. Temes, Water analysis: emerging contaminants and current issues, *Anal. Chem.* 90 (2018) 398–428, <https://doi.org/10.1021/acs.analchem.7b04577>.
- [9] D. Coleman, N. Gathergood, Biodegradation studies of ionic liquids, *Chem. Soc. Rev.* 39 (2010) 600–637, <https://doi.org/10.1039/b817717c>.
- [10] E.M. Siedlecka, W. Mroziak, Z. Kaczynski, P. Stepnowski, Degradation of 1-butyl-3-methylimidazolium chloride ionic liquid in a Fenton-like system, *J. Hazard. Mater.* 154 (2008) 893–900, <https://doi.org/10.1016/j.jhazmat.2007.10.104>.
- [11] H.M. Zhou, Y.Y. Shen, P. Lv, J.J. Wang, J. Fan, Degradation of 1-butyl-3-methylimidazolium chloride ionic liquid by ultrasound and zero-valent iron/activated carbon, *Sep. Purif. Technol.* 104 (2013) 208–213, <https://doi.org/10.1016/j.seppur.2012.11.029>.
- [12] E.A. Serna-Galvis, J. Silva-Agredo, A.L. Giraldo, O.A. Florez-Acosta, R.A. Torres-Palma, Comparative study of the effect of pharmaceutical additives on the elimination of antibiotic activity during the treatment of oxacillin in water by the photo-Fenton, TiO<sub>2</sub>-photocatalysis and electrochemical processes, *Sci. Total Environ.* 541 (2016) 1431–1438, <https://doi.org/10.1016/j.scitotenv.2015.10.029>.
- [13] J.-C.E. Yang, M.-P. Zhu, X. Duan, S. Wang, B. Yuan, M.-L. Fu, The mechanistic difference of 1T-2H MoS<sub>2</sub> homojunctions in persulfates activation: Structure-dependent oxidation pathways, *Appl. Catal. B: Environ.* 297 (2021), 120460, <https://doi.org/10.1016/j.apcatb.2021.120460>.
- [14] A. Ait El Fakir, Z. Anfar, A. Amedlous, M. Zbair, Z. Hafidi, M. El Achouri, A. Jada, N. El Alem, Engineering of new hydrogel beads based conducting polymers: metal-free catalysis for highly organic pollutants degradation, *Appl. Catal. B: Environ.* 286 (2021), 119948, <https://doi.org/10.1016/j.apcatb.2021.119948>.
- [15] A. Babunpusami, K. Muthukumar, Advanced oxidation of phenol: a comparison between Fenton, electro-Fenton, sono-electro-Fenton and photo-electro-Fenton processes, *Chem. Eng. J.* 183 (2012) 1–9, <https://doi.org/10.1016/j.cej.2011.12.010>.
- [16] A. Karci, I. Arslan-Alaton, T. Olmez-Hanci, M. Bekbolet, Transformation of 2,4-dichlorophenol by H<sub>2</sub>O<sub>2</sub>/UV-C, Fenton and photo-Fenton processes: oxidation products and toxicity evolution, *J. Photochem. Photobiol. A* 230 (2012) 65–73, <https://doi.org/10.1016/j.jphotochem.2012.01.003>.
- [17] J. Mendez-Diaz, M. Sanchez-Polo, J. Rivera-Utrilla, S. Canonica, U. von Gunten, Advanced oxidation of the surfactant SDBS by means of hydroxyl and sulphate radicals, *Chem. Eng. J.* 163 (2010) 300–306, <https://doi.org/10.1016/j.cej.2010.08.002>.
- [18] R. Matta, S. Tili, S. Chiron, S. Barbat, Removal of carbamazepine from urban wastewater by sulfate radical oxidation, *Environ. Chem. Lett.* 9 (2011) 347–353, <https://doi.org/10.1007/s10311-010-0285-z>.

- [19] K.-Y.A. Lin, Z.-Y. Zhang, Degradation of Bisphenol A using peroxymonosulfate activated by one-step prepared sulfur-doped carbon nitride as a metal-free heterogeneous catalyst, *Chem. Eng. J.* 313 (2017) 1320–1327, <https://doi.org/10.1016/j.cej.2016.11.025>.
- [20] O. Tantawi, A. Baalbaki, R. El Asmar, A. Ghauch, A rapid and economical method for the quantification of hydrogen peroxide ( $H_2O_2$ ) using a modified HPLC apparatus, *Sci. Total Environ.* 654 (2019) 107–117, <https://doi.org/10.1016/j.scitotenv.2018.10.372>.
- [21] A. Baalbaki, N.Z. Eddine, S. Jaber, M. Amasha, A. Ghauch, Rapid quantification of persulfate in aqueous systems using a modified HPLC unit, *Talanta* 178 (2018) 237–245, <https://doi.org/10.1016/j.talanta.2017.09.036>.
- [22] A. Ghauch, A.M. Tuqan, Oxidation of bisoprolol in heated persulfate/ $H_2O$  systems: kinetics and products, *Chem. Eng. J.* 183 (2012) 162–171, <https://doi.org/10.1016/j.cej.2011.12.048>.
- [23] A. Ghauch, A.M. Tuqan, N. Kibbi, Ibuprofen removal by heated persulfate in aqueous solution: a kinetics study, *Chem. Eng. J.* 197 (2012) 483–492, <https://doi.org/10.1016/j.cej.2012.05.051>.
- [24] G. Ayoub, A. Ghauch, Assessment of bimetallic and trimetallic iron-based systems for persulfate activation: application to sulfamethoxazole degradation, *Chem. Eng. J.* 256 (2014) 280–292, <https://doi.org/10.1016/j.cej.2014.07.002>.
- [25] A. Ghauch, G. Ayoub, S. Naim, Degradation of sulfamethoxazole by persulfate assisted micrometric  $Fe^0$  in aqueous solution, *Chem. Eng. J.* 228 (2013) 1168–1181, <https://doi.org/10.1016/j.cej.2013.05.045>.
- [26] R. El Asmar, A. Baalbaki, Z. Abou Khalil, S. Naim, A. Bejjani, A. Ghauch, Iron-based metal organic framework MIL-88-A for the degradation of naproxen in water through persulfate activation, *Chem. Eng. J.* 405 (2021), 126701, <https://doi.org/10.1016/j.cej.2020.126701>.
- [27] S. Al Hakim, S. Jaber, N.Z. Eddine, A. Baalbaki, A. Ghauch, Degradation of theophylline in a UV254/PS system: matrix effect and application to a factory effluent, *Chem. Eng. J.* 380 (2020), 122478, <https://doi.org/10.1016/j.cej.2019.122478>.
- [28] R.L. Johnson, P.G. Tratnyek, R.O.B. Johnson, Persulfate persistence under thermal activation conditions, *Environ. Sci. Technol.* 42 (2008) 9350–9356, <https://doi.org/10.1021/es8019462>.
- [29] M. Amasha, A. Baalbaki, A. Ghauch, A comparative study of the common persulfate activation techniques for the complete degradation of an NSAID: the case of ketoprofen, *Chem. Eng. J.* 350 (2018) 395–410, <https://doi.org/10.1016/j.cej.2018.05.118>.
- [30] A. Ghauch, A.M. Tuqan, N. Kibbi, Naproxen abatement by thermally activated persulfate in aqueous systems, *Chem. Eng. J.* 279 (2015) 861–873, <https://doi.org/10.1016/j.cej.2015.05.067>.
- [31] H. Hori, Y. Nagano, M. Murayama, K. Koike, S. Kutsuna, Efficient decomposition of perfluorooether carboxylic acids in water with a combination of persulfate oxidant and ultrasonic irradiation, *J. Fluor. Chem.* 141 (2012) 5–10, <https://doi.org/10.1016/j.jfluchem.2012.05.012>.
- [32] A. Ghauch, A. Baalbaki, M. Amasha, R. El Asmar, O. Tantawi, Contribution of persulfate in UV-254 nm activated systems for complete degradation of chloramphenicol antibiotic in water, *Chem. Eng. J.* 317 (2017) 1012–1025, <https://doi.org/10.1016/j.cej.2017.02.133>.
- [33] M. Amasha, A. Baalbaki, S.A. Hakim, R.E. Asmar, A. Ghauch, Degradation of a toxic molecule o-toluidine in industrial effluents using UV254/PS system, *J. Adv. Oxid. Technol.* 21 (2018) 261–273, <https://doi.org/10.26802/jaots.2017.0099>.
- [34] S. Al Hakim, A. Baalbaki, O. Tantawi, A. Ghauch, Chemically and thermally activated persulfate for theophylline degradation and application to pharmaceutical factory effluent, *RSC Adv.* 9 (2019) 33472–33485, <https://doi.org/10.1039/c9ra05362j>.
- [35] S. Naim, A. Ghauch, Ranitidine abatement in chemically activated persulfate systems: assessment of industrial iron waste for sustainable applications, *Chem. Eng. J.* 288 (2016) 276–288, <https://doi.org/10.1016/j.cej.2015.11.101>.
- [36] X. Zhou, M. Luo, C. Xie, H. Wang, J. Wang, Z. Chen, J. Xiao, Z. Chen, Tunable S doping from  $Co_3O_4$  to  $Co_9S_8$  for peroxymonosulfate activation: Distinguished Radical/Nonradical species and generation pathways, *Appl. Catal. B: Environ.* 282 (2021), 119605, <https://doi.org/10.1016/j.apcatb.2020.119605>.
- [37] L. Ismail, C. Ferronato, L. Fine, F. Jaber, J.-M. Chovelon, Elimination of sulfaclozine from water with  $SO_4^{\cdot-}$  radicals: evaluation of different persulfate activation methods, *Appl. Catal. B-Environ.* 201 (2017) 573–581, <https://doi.org/10.1016/j.apcatb.2016.08.046>.
- [38] X.Y. Wang, A.Q. Wang, J. Ma, Visible-light-driven photocatalytic removal of antibiotics by newly designed  $C_3N_4@MnFe_2O_4$ -graphene nanocomposites, *J. Hazard. Mater.* 336 (2017) 81–92, <https://doi.org/10.1016/j.jhazmat.2017.04.012>.
- [39] W. Xiang, Q. Ji, C. Xu, Y. Guo, Y. Liu, D. Sun, W. Zhou, Z. Xu, C. Qi, S. Yang, S. Li, C. Sun, H. He, Accelerated photocatalytic degradation of iohexol over  $Co_3O_4/g-C_3N_4/Bi_2O_3CO_3$  of p-n/n-n dual heterojunction under simulated sunlight by persulfate, *Appl. Catal. B: Environ.* 285 (2021), 119847, <https://doi.org/10.1016/j.apcatb.2020.119847>.
- [40] Q. Yang, Y. Ma, F. Chen, F. Yao, J. Sun, S. Wang, K. Yi, L. Hou, X. Li, D. Wang, Recent advances in photo-activated sulfate radical-advanced oxidation process (SR-AOP) for refractory organic pollutants removal in water, *Chem. Eng. J.* 378 (2019), 122149, <https://doi.org/10.1016/j.cej.2019.122149>.
- [41] R. Dewil, D. Mantzavinos, I. Poullos, M.A. Rodrigo, New perspectives for advanced oxidation processes, *J. Environ. Manag.* 195 (2017) 93–99, <https://doi.org/10.1016/j.jenvman.2017.04.010>.
- [42] S. Mukherjee, F. Libisch, N. Large, O. Neumann, L.V. Brown, J. Cheng, J.B. Lassiter, E.A. Carter, P. Nordlander, N.J. Halas, Hot electrons do the impossible: plasmon-induced dissociation of  $H_2$  on Au, *Nano Lett.* 13 (2013) 240–247, <https://doi.org/10.1021/nl303940z>.
- [43] S. Mukherjee, L. Zhou, A.M. Goodman, N. Large, C. Ayala-Orozco, Y. Zhang, P. Nordlander, N.J. Halas, Hot-electron-induced dissociation of  $H_2$  on gold nanoparticles supported on  $SiO_2$ , *J. Am. Chem. Soc.* 136 (2014) 64–67, <https://doi.org/10.1021/ja411017b>.
- [44] J. Guo, Y. Zhang, L. Shi, Y. Zhu, M.F. Mideksa, K. Hou, W. Zhao, D. Wang, M. Zhao, X. Zhang, J. Lv, J. Zhang, X. Wang, Z. Tang, Boosting hot electrons in hetero-superstructures for plasmon-enhanced catalysis, *J. Am. Chem. Soc.* 139 (2017) 17964–17972, <https://doi.org/10.1021/jacs.7b08903>.
- [45] P. Christopher, H. Xin, S. Linic, Visible-light-enhanced catalytic oxidation reactions on plasmonic silver nanostructures, *Nat. Chem.* 3 (2011) 467–472, <https://doi.org/10.1038/nchem.1032>.
- [46] F. Wang, C. Li, H. Chen, R. Jiang, L.-D. Sun, Q. Li, J. Wang, J.C. Yu, C.-H. Yan, Plasmonic harvesting of light energy for suzuki coupling reactions, *J. Am. Chem. Soc.* 135 (2013) 5588–5601, <https://doi.org/10.1021/ja310501y>.
- [47] H.-K. Choi, W.-H. Park, C.-G. Park, H.-H. Shin, K.S. Lee, Z.H. Kim, Metal-catalyzed chemical reaction of single molecules directly probed by vibrational spectroscopy, *J. Am. Chem. Soc.* 138 (2016) 4673–4684, <https://doi.org/10.1021/jacs.6b01865>.
- [48] A.R. Siekkinen, J.M. McLellan, J. Chen, Y. Xia, Rapid synthesis of small silver nanocubes by mediating polyol reduction with a trace amount of sodium sulfide or sodium hydrosulfide, *Chem. Phys. Lett.* 432 (2006) 491–496, <https://doi.org/10.1016/j.cplett.2006.10.095>.
- [49] U. Aslam, S. Chavez, S. Linic, Controlling energy flow in multimetallic nanostructures for plasmonic catalysis, *Nat. Nanotechnol.* 12 (2017) 1000–1005, <https://doi.org/10.1038/nnano.2017.131>.
- [50] U. Aslam, S. Linic, Addressing challenges and scalability in the synthesis of thin uniform metal shells on large metal nanoparticle cores: case study of Ag-Pt core-shell nanocubes, *ACS Appl. Mater. Interfaces* 9 (2017) 43127–43132, <https://doi.org/10.1021/acsami.7b14474>.
- [51] E.D. Palik, *Handbook of Optical Constants of Solid*, Academic Press., New York, 1985.
- [52] Y. Wu, X. Sun, Y. Yang, J. Li, Y. Zhang, D. Qin, Enriching silver nanocrystals with a second noble metal, *Acc. Chem. Res.* 50 (2017) 1774–1784, <https://doi.org/10.1021/acs.accounts.7b00216>.
- [53] K.D. Gilroy, A. Ruditskiy, H.C. Peng, D. Qin, Y.N. Xia, Bimetallic nanocrystals: syntheses, properties, and applications, *Chem. Rev.* 116 (2016) 10414–10472, <https://doi.org/10.1021/acs.chemrev.6b00211>.
- [54] J.F. Moulder, W.F. Stickle, P.E. Sobol, K.D. Bomben, *Handbook of X ray photoelectron spectroscopy: a reference book of standard spectra for identification and interpretation of XPS data*, Phys. Electron.; Reissue Ed. (1995).
- [55] T.S. Rodrigues, M. Zhao, T.-H. Yang, K.D. Gilroy, A.G.M. da Silva, P.H.C. Camargo, Y. Xia, Synthesis of colloidal metal nanocrystals: a comprehensive review on the reductants, *Chem. Eur. J.* 24 (2018) 16944–16963, <https://doi.org/10.1002/chem.201802194>.
- [56] S. Stolte, J. Arning, U. Bottin-Weber, A. Müller, W.-R. Pitner, U. Welz-Biermann, B. Jastorff, J. Ranke, Effects of different head groups and functionalised side chains on the cytotoxicity of ionic liquids, *Green. Chem.* 9 (2007) 760–767, <https://doi.org/10.1039/b615326g>.
- [57] W.-D. Oh, Z. Dong, T.-T. Lim, Generation of sulfate radical through heterogeneous catalysis for organic contaminants removal: current development, challenges and prospects, *Appl. Catal. B-Environ.* 194 (2016) 169–201, <https://doi.org/10.1016/j.apcatb.2016.04.003>.
- [58] J. Lee, U. von Gunten, J.H. Kim, Persulfate-based advanced oxidation: critical assessment of opportunities and roadblocks, *Environ. Sci. Technol.* 54 (2020) 3064–3081, <https://doi.org/10.1021/acs.est.9b07082>.
- [59] N. Hasan, S. Kim, M.S. Kim, N. Nguyen Thi Thao, C. Lee, J. Kim, Visible light-induced activation of peroxymonosulfate in the presence of ferric ions for the degradation of organic pollutants, *Sep. Purif. Technol.* 240 (2020), 116620, <https://doi.org/10.1016/j.seppur.2020.116620>.
- [60] H. Guo, S. Su, Y. Liu, X. Ren, W. Guo, Enhanced catalytic activity of MIL-101(Fe) with coordinatively unsaturated sites for activating persulfate to degrade organic pollutants, *Environ. Sci. Pollut. Res.* 27 (2020) 17194–17204, <https://doi.org/10.1007/s11356-020-08316-z>.
- [61] X. Zhong, Z.-S. Zou, H.-L. Wang, W. Huang, B.-X. Zhou, Enhanced activation of persulfate by Co-doped bismuth ferrite nanocomposites for degradation of levofloxacin under visible light irradiation, *Materials (Basel, Switzerland)* 12 (2019) 3952, <https://doi.org/10.3390/ma12233952>.
- [62] L. Chen, D. Ding, C. Liu, H. Cai, Y. Qu, S. Yang, Y. Gao, T. Cai, Degradation of norfloxacin by  $CoFe_2O_4$ -GO composite coupled with peroxymonosulfate: a comparative study and mechanistic consideration, *Chem. Eng. J.* 334 (2018) 273–284, <https://doi.org/10.1016/j.cej.2017.10.040>.
- [63] Y. Gao, Z. Zhang, S. Li, J. Liu, L. Yao, Y. Li, H. Zhang, Insights into the mechanism of heterogeneous activation of persulfate with a clay/iron-based catalyst under visible LED light irradiation, *Appl. Catal. B-Environ.* 185 (2016) 22–30, <https://doi.org/10.1016/j.apcatb.2015.12.002>.
- [64] W. Li, Y.X. Li, D.Y. Zhang, Y.Q. Lan, J. Guo,  $CuO-Co_3O_4@CeO_2$  as a heterogeneous catalyst for efficient degradation of 2,4-dichlorophenoxyacetic acid by peroxymonosulfate, *J. Hazard. Mater.* 381 (2020), 121209, <https://doi.org/10.1016/j.jhazmat.2019.121209>.
- [65] R. Zhou, J. Zhao, N.F. Shen, T.G. Ma, Y. Su, H.J. Ren, Efficient degradation of 2,4-dichlorophenol in aqueous solution by peroxymonosulfate activated with magnetic spinel  $FeCo_2O_4$  nanoparticles, *Chemosphere* 197 (2018) 670–679, <https://doi.org/10.1016/j.chemosphere.2018.01.079>.
- [66] J. Li, Y. Ren, F.Z. Ji, B. Lai, Heterogeneous catalytic oxidation for the degradation of p-nitrophenol in aqueous solution by persulfate activated with  $CuFe_2O_4$

- magnetic nano-particles, *Chem. Eng. J.* 324 (2017) 63–73, <https://doi.org/10.1016/j.cej.2017.04.104>.
- [67] M.Y. Sun, Y. Lei, H. Cheng, J.F. Ma, Y. Qin, Y. Kong, S. Komarneni, Mg doped CuO-Fe<sub>2</sub>O<sub>3</sub> composites activated by persulfate as highly active heterogeneous catalysts for the degradation of organic pollutants, *J. Alloy. Compd.* 825 (2020), 154036, <https://doi.org/10.1016/j.jallcom.2020.154036>.
- [68] S.-S. Wang, W.-C. Hu, F.-F. Liu, Q.-Y. Xu, C. Wang, Insights into direct plasmon-activated electrocatalysis on gold nanostar via efficient photothermal effect and reduced activation energy, *Electrochim. Acta* 301 (2019) 359–365, <https://doi.org/10.1016/j.electacta.2019.01.172>.
- [69] M. Kim, M. Lin, J. Son, H. Xu, J.-M. Nam, Hot-electron-mediated photochemical reactions: principles, recent advances, and challenges, *Adv. Opt. Mater.* 5 (2017), 1700004, <https://doi.org/10.1002/adom.201700004>.
- [70] S. Yu, A.J. Wilson, G. Kumari, X. Zhang, P.K. Jain, Opportunities and challenges of solar-energy-driven carbon dioxide to fuel conversion with plasmonic catalysts, *ACS Energy Lett.* 2 (2017) 2058–2070, <https://doi.org/10.1021/acsenergylett.7b00640>.
- [71] M. Bernardi, J. Mustafa, J.B. Neaton, S.G. Louie, Theory and computation of hot carriers generated by surface plasmon polaritons in noble metals, *Nat. Commun.* 6 (2015) 7044, <https://doi.org/10.1038/ncomms8044>.
- [72] W. Hou, W.H. Hung, P. Pavaskar, A. Goepfert, M. Aykol, S.B. Cronin, Photocatalytic conversion of CO<sub>2</sub> to hydrocarbon fuels via plasmon-enhanced absorption and metallic interband transitions, *ACS Catal.* 1 (2011) 929–936, <https://doi.org/10.1021/cs2001434>.
- [73] S. Chavez, V.G. Rao, S. Linic, Unearthing the factors governing site specific rates of electronic excitations in multicomponent plasmonic systems and catalysts, *Faraday Discuss.* 214 (2019) 441–453, <https://doi.org/10.1039/c8fd00143j>.
- [74] E. Bocos, E. Gonzalez-Romero, M. Pazos, M. Angeles Sanroman, Application of electro-Fenton treatment for the elimination of 1-butyl-3-methylimidazolium triflate from polluted water, *Chem. Eng. J.* 318 (2017) 19–28, <https://doi.org/10.1016/j.cej.2016.04.058>.
- [75] H. Zhou, Y. Shen, P. Lv, J. Wang, P. Li, Degradation pathway and kinetics of 1-alkyl-3-methylimidazolium bromides oxidation in an ultrasonic nanoscale zero-valent iron/hydrogen peroxide system, *J. Hazard. Mater.* 284 (2015) 241–252, <https://doi.org/10.1016/j.jhazmat.2014.10.050>.
- [76] E. Bocos, M. Pazos, M. Angeles Sanroman, Electro-Fenton treatment of imidazolium-based ionic liquids: kinetics and degradation pathways, *RSC Adv.* 6 (2016) 1958–1965, <https://doi.org/10.1039/c5ra24070k>.
- [77] H.M. Zhou, P. Lv, Y.Y. Shen, J.J. Wang, J. Fan, Identification of degradation products of ionic liquids in an ultrasound assisted zero-valent iron activated carbon micro-electrolysis system and their degradation mechanism, *Water Res.* 47 (2013) 3514–3522, <https://doi.org/10.1016/j.watres.2013.03.057>.
- [78] M. Munoz, C.M. Dominguez, Z.M. de Pedro, A. Quintanilla, J.A. Casas, J. Rodriguez, Ionic liquids breakdown by Fenton oxidation, *Catal. Today* 240 (2015) 16–21, <https://doi.org/10.1016/j.cattod.2014.03.028>.
- [79] Y.W. Gao, S.M. Li, Y.X. Li, L.Y. Yao, H. Zhang, Accelerated photocatalytic degradation of organic pollutant over metal-organic framework MIL-53(Fe) under visible LED light mediated by persulfate, *Appl. Catal. B-Environ.* 202 (2017) 165–174, <https://doi.org/10.1016/j.apcatb.2016.09.005>.